remote sensing

MDPI

Article

Characterization of 77 GHz Radar Backscattering from Sea Surfaces at Low Incidence Angles: Preliminary Results

Qinghui Xu [1], Chen Zhao [1,2,*], Zezong Chen [1], Sitao Wu [1], Xiao Wang [1] and Lingang Fan [3]

[1] School of Electronic Information, Wuhan University, Wuhan 430072, China; qinghuixu@whu.edu.cn (Q.X.); chenzz@whu.edu.cn (Z.C.); sitaowhu@whu.edu.cn (S.W.); wangxiao1124@whu.edu.cn (X.W.)
[2] Donghai Laboratory, Zhoushan 316021, China
[3] Beijing Institute of Radio Measurement, Beijing 100854, China; flg2004@163.com
* Correspondence: zhaoc@whu.edu.cn

Abstract: Millimeter-wave (MMW) radar is capable of providing high temporal–spatial measurements of the ocean surface. Some topics, such as the characterization of the radar echo, have attracted widespread attention from researchers. However, most existing research studies focus on the backscatter of the ocean surface at low microwave bands, while the sea surface backscattering mechanism in the 77 GHz frequency band remains not well interpreted. To address this issue, in this paper, the investigation of the scattering mechanism is carried out for the 77 GHz frequency band ocean surface at small incidence angles. The backscattering coefficient is first simulated by applying the quasi-specular scattering model and the corrected scattering model of geometric optics (GO4), using two different ocean wave spectrum models (the Hwang spectrum and the Kudryavtsev spectrum). Then, the dependence of the sea surface normalized radar cross section (NRCS) on incidence angles, azimuth angles, and sea states are investigated. Finally, by comparison between model simulations and the radar-measured data, the 77 GHz frequency band scattering characterization of sea surfaces at the near-nadir incidence is verified. In addition, experimental results from the wave tank are shown, and the difference in the scattering mechanism is further discussed between water surfaces and oceans. The obtained results seem promising for a better understanding of the ocean surface backscattering mechanism in the MMW frequency band. It provides a new method for fostering the usage of radar technologies for real-time ocean observations.

Keywords: millimeter wave; ocean observations; low incidence; quasi-specular scattering

check for updates

Academic Editor: Martin Gade

Received: 5 November 2024
Revised: 20 December 2024
Accepted: 31 December 2024
Published: 1 January 2025

Citation: Xu, Q.; Zhao, C.; Chen, Z.; Wu, S.; Wang, X.; Fan, L. Characterization of 77 GHz Radar Backscattering from Sea Surfaces at Low Incidence Angles: Preliminary Results. *Remote Sens.* **2025**, *17*, 116. https://doi.org/10.3390/rs17010116

Copyright: © 2025 by the authors. Licensee MDPI, Basel, Switzerland. This article is an open access article distributed under the terms and conditions of the Creative Commons Attribution (CC BY) license (https://creativecommons.org/licenses/by/4.0/).

1. Introduction

For the past few years, with the rapid development of 6G communication technologies, especially integrated sensing and communication using wireless networks [1], the millimeter-wave (MMW) frequency band has attracted more and more attention from researchers in the field of communication and radar. On the one hand, due to the advantages of high temporal–spatial observations, compact size, and relatively low power consumption, the MMW radar can detect targets with higher accuracy and has been used in various fields, for example, self-driving cars [2], intelligent security systems, and so on. On the other hand, because of the complexity of wave motion, sea surface investigation is a challenging task, as exemplified in the studies of sea echo models [3–5] and the inversion of wave parameters [6,7]. The air/space-based MMW radar is able to provide new insights for increased accuracy in ocean surface observations, and it has the potential to supply security for maritime activities, such as ship navigation and rescue at sea.

Up until the present, the study on the sea surface scattering of the MMW frequency band has been mainly focused on the Ka band. Based on the Ka-band radar, some experiments were performed in wind–wave tanks [8–11] and on ocean observations with the radar mounted on the coast [12–14], plane or satellite [15–18]. In the wind–wave tank experiment, Plant et al. [19,20] proved the dominant role of bound capillary waves in the scattering process in the Ka band, and it was affected by friction velocity on the sea surface. The backscattering of the sea surface was investigated by Karaev et al. [21] for the transition range of incidence angles within the framework of the two-scale model, and the new mode interpreted a decrease in the Bragg components at low incidence angles. Bringer et al. [22] researched the peakedness effects in view of the limitations of the geometrical optics (GO) approximation and the multiscale and non-Gaussian nature of the surface, and the proposed model was verified based on the Ka-band radar datasets in near-nadir observations. To explore the scattering mechanism at small incidence, Boisot et al. [23] carried out a study of the normalized radar cross section (NRCS) by observations in a wind–wave tank and modeling of Ka-band scattering from the water surface, and the scattering coefficient was analyzed for various wind speeds and scattering angles. The sea surface backscattering characteristics in the near-nadir region were also modeled and described under different conditions, such as the modification of relative permittivity by air in foam and whitecaps [24], the sea surface wind, wave, and temperature parameters [25]. Some scattering models, such as the physical optics (PO) model, the GO model [26], the corrected scattering model of the GO (GO4) [27], and the full-polarized facet-based scattering model [28], have been proposed to describe the scattering mechanism of the marine environment with a simplified formula and intelligible physical process. The research on Ka-band sea surface backscattering at moderate incidence angles has also received extensive attention by researchers. The backscattering features of the sea surface were studied by Yurovsky [29] using the dual-copolarized Ka-band radar. Meanwhile, the effective NRCS of breaking waves was estimated using a Ka-band continuous-wave radar and a video camera [30].

In addition to the Ka band, sea surface backscattering in the W band has also been studied. Horie et al. [31] explored the NRCS of the sea surface in near-nadir for relatively diverse wind speeds at W-band frequency. Li et al. [32] conducted the measurements of the ocean surface backscattering under a variety of wind conditions using a 94 GHz cloud radar, and the results showed that the NRCS was insensitive to wind conditions near a 10° incidence angle. Battaglia et al. [33] presented the measurement results of the W-band NRCS for vertical and horizontal polarization at moderate incidence angles, and the second-order small-slope approximation (SSA2) theory was used to estimate the polarimetric scattering signature of the sea surface. However, the phenomenon and mechanism involved in near-nadir-radar observations for electromagnetic radiation at 77 GHz frequency are still not well studied. Therefore, the interpretation of the scattering mechanism and data from sea surfaces in the 77 GHz frequency band requires further improvement.

Furthermore, since a majority of MMW radars are deployed on air/space-based platforms (e.g., aircraft and satellites), the scattering mechanism at near vertical incidence plays an essential role in the investigation of sea surfaces. In this paper, to study the 77 GHz radar return from sea surfaces at the near-nadir incidence, the scattering mechanism was analyzed under different incidence angles, azimuth angles, and sea states by employing the quasi-specular (QS) model [34] and the GO4 model. Then, ocean observations and wave tank experiments were carried out using a 77 GHz radar at the near-nadir incidence. The abilities of the QS model and GO4 model to reproduce the small-incidence NRCS were compared in the ocean observation. In addition, the difference in the scattering mechanism was analyzed between marine environments and water surfaces. The obtained results

provide a better understanding of the MMW-frequency-band ocean surface backscattering mechanism at low incidence angles.

The rest of this article is organized as follows. The observations and radar data processing are introduced in Section 2. The scattering model and wave spectrum are described in the MMW frequency band in Section 3. In Section 4, the scattering mechanism is analyzed by combining the measured data with the theoretical simulation. Moreover, the difference in scattering characterization between wave tank experiments and oceans is compared, and the results are discussed. Finally, the conclusions and future work are presented in Section 5.

2. Experiments and Data Processing

To study the scattering mechanism of the 77 GHz frequency band at small incidence angles, a wave tank experiment and a sea trial were conducted using a MMW radar. Figure 1 illustrates the geometry for MMW radar observations. The radar was installed in a nadir-looking mode, and the radar antenna footprint area covers a patch of water or ocean surfaces below. θ is the incidence angle; h is the radar height; r_0 denotes the shortest distance, which can also be considered as the path length when the electromagnetic wave is perpendicular to the water or ocean surface; and r_1 expresses the path range of the incident electromagnetic wave at an incidence angle θ.

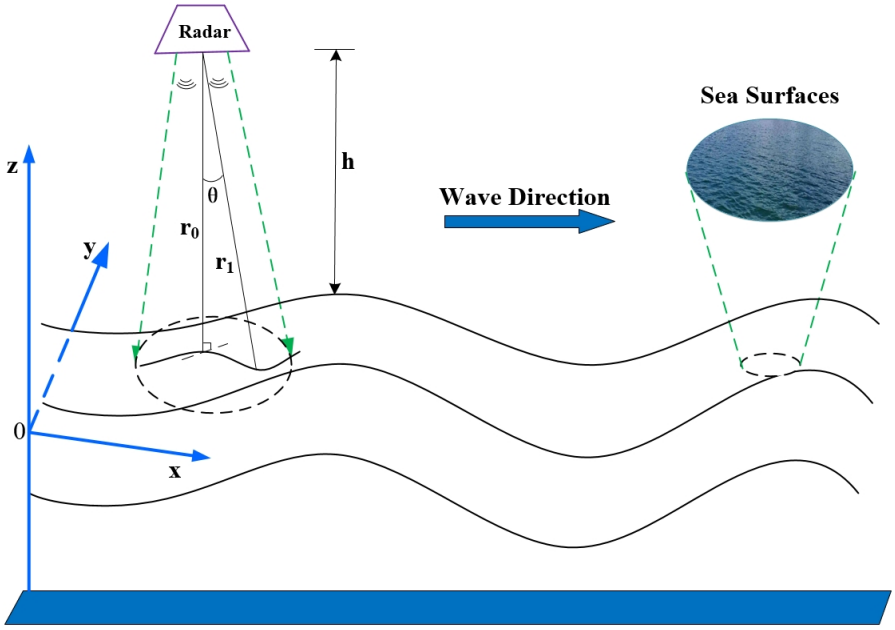


Figure 1. The geometry for MMW radar observations.

2.1. MMW Radar

The observation equipment used is the AWR2243 cascade radar board by TI company, including the RF front-end board and the digital signal processing board. The MMW radar operates at 77 GHz, corresponding to an approximate wavelength of 3.9 mm. It adopts frequency-modulated continuous wave (FMCW) chirps for radio energy radiation, and signals are transmitted and received by a microstrip antenna array (four radiating elements). The receiving and transmitting antenna arrays contain 16 and 12 channels, respectively, which work in the time-division multiplexing (TDM) mode, and the Multiple-Input Multiple-Output (MIMO) is also applied to obtain the radar echo signal. Based on the space between transmitting and receiving antennas, the 12 $\times$ 16 MIMO is equivalent to a virtual array of 192 antennas (channels). Because of adopting a virtual array, the MMW radar uses a digital beamforming technique to obtain high angular resolution. The 3 dB

beamwidth of the receiving antenna array is about 1.4° in the azimuth field of view, and about 18° in the elevation field of view. The main electrical radar parameters used for sea surface experiments are listed in Table 1.

Table 1. The MMW radar parameters for the sea surface experiment.

Parameter	Value	Unit
Operating frequency	77	GHz
Bandwidth	1.5	GHz
RF gain target	48	dB
Azimuth field of view	±60	[°]
Elevation field of view	±30	[°]
ADC sampling	512	
Range resolution	0.1	m

2.2. Ocean Observations

To investigate the sea surface scattering characterization in the MMW frequency band, ocean observations were conducted in December 2023 and July 2024, near the coast of Qingdao, Shandong Province, China. Compared to shipborne, airborne, and spaceborne platforms, unmanned aerial vehicles (UAVs) are low-cost platforms that have unique capabilities to access inaccessible environments in quick turnaround times. In the sea surface experiments, the MMW radar was installed under the UAV in the nadir-looking mode, and emitted electromagnetic waves that were incident vertically on the ocean surface. A wave buoy (Waverider MKIII) was deployed to provide wave parameters, e.g., significant wave height, mean wave period, and wave direction. Figure 2 shows the set-up of the MMW radar measurements over the ocean. The red circle indicates the site of the wave buoy. The device in the blue circle is the UAV with the MMW radar. The hovering position of the UAV was above the location near the wave buoy. For sea surface observations, six UAV flights were carried out, every measurement lasted around 15 min, and the radar worked continuously and collected ocean surface echo data. The details of the used datasets are given in Table 2.

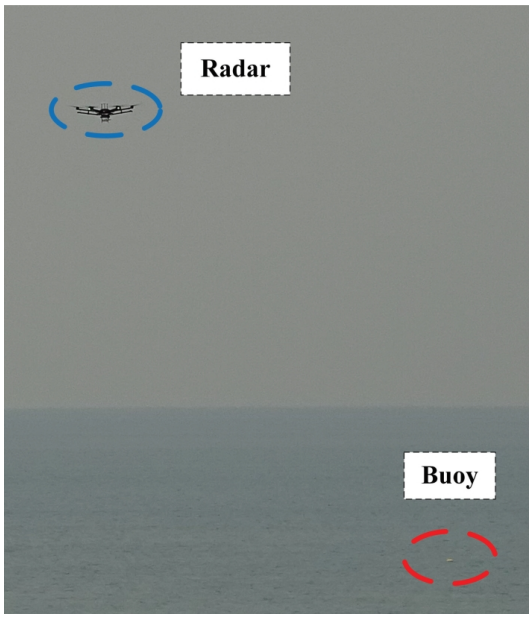


Figure 2. Experimental set-up for sea surface observations. The device in the blue circle is the UAV with the MMW radar. The red circle is the site of the wave buoy.

Table 2. Experimental data in ocean surface measurements.

Significant Wave Height (m)	Wave Period (s)	Wave Direction (°)	Wind Speed (m/s)	Number of Data Samples
0.33	4.10	167.3	3.1	109,120
0.40	4.80	173.0	3.5	109,120
0.43	2.20	0.3	3.7	87,296
0.48	2.43	3.9	4.1	109,120
0.52	2.94	0.1	4.3	87,296
0.63	4.20	158.0	5.1	109,120

2.3. Wave Tank Observations

To compare the difference in scattering mechanism between ocean surfaces and the water surface in the 77 GHz frequency band, a wave tank experiment was carried out in October 2023. The wave tank with a size of 50 m (long) × 30 m (wide) × 10 m (deep) was built indoors without the influence of the wind. The undulating waves, including regular waves (i.e., sine-shaped waves) and irregular waves (the energy of the water surfaces is close to the JONSWAP spectrum), could be generated by configuring the wave generator of the wave tank. The MMW radar was mounted on the stationary bridge at a height of about 13.5 m above the water surface in a nadir-looking mode. The radar pointed downward at an area located at the center of the water tank. Figure 3 shows the MMW radar installation in the wave tank experiment. Based on the wave tank, five experiments were performed, i.e., the regular waves with peak-to-peak heights of 0.15 m and 0.34 m, and the irregular waves with significant wave heights (H_s) of 0.16 m, 0.19 m, and 0.24 m, respectively. The produced regular waves lasted about 2 min, and the irregular waves lasted approximately 4 min. The above five configurations provided the different water surface environments for the MMW radar, and then the observation data were collected. The experimental data used are shown in Table 3.



Figure 3. Experimental set-up in the wave tank. The radar was fixed on the stationary red bridge at a height of about 13.5 m.

Table 3. Experimental data from the wave tank measurements.

Type	Wave Height (m)	Wave Period (s)	Number of Data Samples
Regular wave	0.15	1.80	38,400
	0.34	1.82	38,400
Irregular wave	0.16	1.60	79,360
	0.19	1.78	79,360
	0.24	1.94	79,360

2.4. Radar Data Processing

In wave tank experiments, the strong reflection from the measurement environment was found in the radar echo signal, and these interference signals had an effect on the accuracy of the experimental measurement. As a result, the signal correction of measured data should be applied in the subsequent processing via the range spectrum.

Raw analog-to-digital converter (ADC) data with multi-dimensional, including samples (fast time) and chirps (slow time), were collected from the wave tank and sea trial experiments. The MMW radar system transmitted twelve FMCW chirps with the same frequency and sweep periods at TDM mode within one sampling period, and received radar backscattered signals modulated by wave motion from water surfaces or sea during the reception time of the total pulse period. The frame data were generated and collected (the frame data were the radar cube data, including the fast time dimension, slow time dimension, and antenna dimension). The range spectrum was estimated from the received raw ADC data using the fast Fourier transform, as shown in Figure 4. For every sample datum, the signals from different incidence angles could be separated by combining digital beamforming and MIMO array techniques. Because of an angular resolution of about 1.4° for the used radar, an incidence angle step of 2° was employed for the real observational data. Then, the signal components at a particular incidence angle were obtained, and the amplitude of signal power was extracted. For real observations, multi-frame ADC data were generated, and then the average amplitude was obtained by averaging the processed multi-frame radar data.

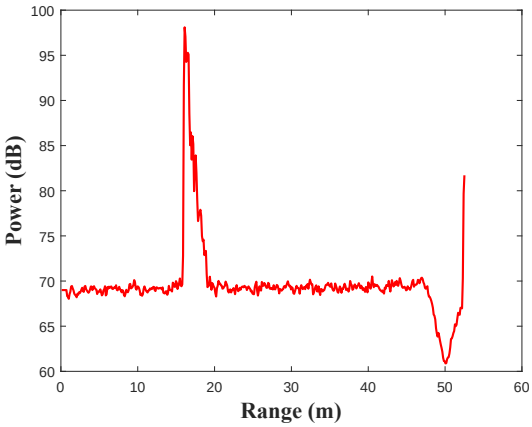


Figure 4. The range spectrum of single-chirp signal for the sea surface observation.

During the ocean surface observation, the UAV maintained a stable hover in the air. The collected results may be influenced by the six-degree-of-freedom motion of the platform. Therefore, an attitude-measuring sensor was placed on the UAV to record the attitude of the UAV (e.g., roll, pitch, and yaw). Among them, the roll angle and pitch angle would affect the observed incidence angles, and the yaw angle would have an effect on the observed azimuth angles. Under low sea states, the attitude data from the sensor showed that most

of the roll, pitch, and yaw angles had a small variation (within 3°). Based on the research in [35,36], after rotation through a pitch angle Ω_P and a roll angle Ω_R (as shown in Figure 5), the unit vector $\hat{k}$ for radar antenna in the propagation direction could be described as in Equation (1), and the new incidence angle θ' is given as in Equation (2). By Equation (2), the incidence angle variation produced by the platform motion was approximately within $\pm 1.5°$, and these variations were used to calibrate the measured NRCS. However, the times from the radar and the sensor in this observation were not aligned. Therefore, the average sample of the sensor during a very short time (1 s) was used to calibrate the single sample from the radar.

$$\begin{aligned}\hat{k} =& \hat{x}(\sin\theta\cos\Omega_R + \cos\theta\sin\Omega_R) + \hat{y}\sin\theta\sin\Omega_P\sin\Omega_R + \\ & \hat{z}(-\sin\theta\cos\Omega_P\sin\Omega_R + \cos\theta\cos\Omega_P\cos\Omega_R)\end{aligned} \tag{1}$$

where $\hat{x}$, $\hat{y}$, and $\hat{z}$ are the three unit vectors from the coordinate system.

$$\theta' = \cos^{-1}(-\sin\theta\cos\Omega_P\sin\Omega_R + \cos\theta\cos\Omega_P\cos\Omega_R). \tag{2}$$

For obtaining the backscattering coefficient from the measurement data, the MMW radar system must be calibrated carefully. The basic form of a radar equation is applied to estimate the backscattered power (P_r) received by the antenna:

$$P_r = \frac{P_t G_t G_r \lambda^2 \sigma}{(4\pi)^3 r^4 L_a L_s} \tag{3}$$

where P_t is the emitted power density; G_t and G_r are the gains of transmit antenna and receive antenna, respectively; λ is the wavelength of the radar wave; σ is the ocean surface radar cross section; r is the distance between the antenna and the rough surface; L_s and L_a are losses from the radar system and the atmosphere; and P_t, G_t, G_r, and λ are the inherent properties of the MMW radar.

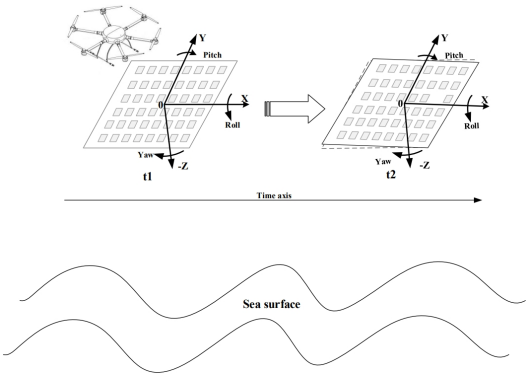


Figure 5. The attitude of the UAV platform.

In our case, an external calibration using a trihedral corner reflector with a known radar cross section σ_i was carried out, and the receiving power P_i was

$$P_i = \frac{P_t G_t G_r \lambda^2 \sigma_i}{(4\pi)^3 r_i^4 L_a L_s}. \tag{4}$$

Therefore, the powers received from the water and sea surfaces were estimated by comparison with the power received from the corner reflector at a known distance in the far field. During this process, the calibration procedure was performed with a 139 mm edge-corner reflector, and the calibration distance had to be as close as possible to the real surface measurement environment. The geometry for the external calibration is shown in Figure 6a.

The UAV with the MMW radar hovered in the air, the trihedral corner reflector was placed on the ground, and the view of the camera in the UAV for measurement environment is shown in Figure 6b. Based on the above analysis, the following relationship is given:

$$\sigma = \frac{P_r r^4 \sigma_i}{P_i r_i^4}. \tag{5}$$

To improve the accuracy of the external calibration, the radar receiving power P_i was processed by averaging the sample data in the external calibration experiment. Furthermore, the error from the radar system was corrected by combining the observation data and calibration experiment. The possible sources of errors in the estimation of the calibration coefficient are approximately ± 0.6 dB, including ± 0.5 dB for the trihedral corner reflector and ± 0.1 dB for the transmission loss.

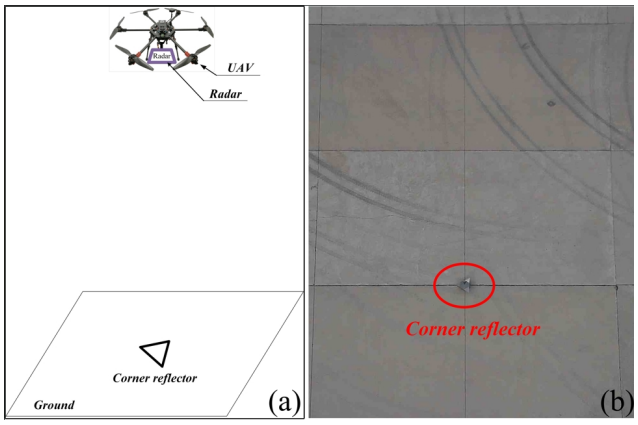


Figure 6. Experimental set-up for the external calibration. (**a**) The geometry for the external calibration. The UAV with the MMW radar hovered in the air, and the trihedral corner reflector was placed on the ground. (**b**) The measurement environment from the view of the camera in the UAV.

Equation (5) gives the obtained ocean surface radar cross section by using an external calibration. For the radar antenna footprint area, the NRCS (σ^0) is evaluated as

$$\sigma^0 = \frac{\sigma}{A_c} \tag{6}$$

where A_c represents the resolution cell area.

3. Theory and Methodology

3.1. Scattering Models

In the MMW frequency band, the QS scattering theory is valid for the investigation of the sea surface scattering mechanism at low incidence angles [32]. The QS scattering model could be obtained using a second-order Taylor expansion of the Kirchhoff approximation stationary phase approximation. The general expression for incidence angles near the nadir can be written as [37,38]

$$\sigma_{QS}^0 = \pi |R|^2 sec^4(\theta) P(X, Y) \tag{7}$$

where R is the normal-incidence Fresnel-reflection coefficient of the sea surface; $P(X, Y)$ is the joint probability density function (PDF) of the sea surface slopes; and X and Y represent two orthogonal directions in ocean surfaces, respectively. $P(X, Y)$ is proportional to the amount of the specular facets observed by the MMW radar. For a perfectly flat sea surface, the theoretical normal incidence MMW-band Fresnel-reflection coefficient is described as $|R| = |(\sqrt{\varepsilon_r} - 1)/(\sqrt{\varepsilon_r} + 1)|$, where ε_r is the dielectric constant of the sea water.

The accurate calculation of the complex dielectric constant ε_r of sea water is necessary for investigating the 77 GHz radar backscattering from sea surfaces. Based on the double Debye relaxation form, the dielectric constant is a function of frequency f (unit: GHz), water temperature T_s (unit: °C), and salinity s (unit: ‰), and the model is given in the following equation:

$$\begin{aligned}\varepsilon_r(T_s,s) = \varepsilon_\infty(T_s,s) + \frac{\varepsilon_s(T_s,s) - \varepsilon_1(T_s,s)}{1 + jf\tau_1(T_s,s)} \\ + \frac{\varepsilon_1(T_s,s) - \varepsilon_\infty(T_s,s)}{1 + jf\tau_2(T_s,s)} - j\frac{\rho(T_s,s)}{2\pi f\varepsilon_0}\end{aligned} \tag{8}$$

where ε_0 is the permittivity of free space ($\varepsilon_0 = 8.8541878 \times 10^{-12}$ F/m); ε_s, ε_1, and ε_∞ are the dielectric constants at zero frequency, an intermediate frequency, and an infinite frequency, respectively; ρ is the ionic conductivity; and τ_1 and τ_2 are the relaxation frequency constants. More details of Equation (8) can be found in the paper by Liu et al. [39]. For the numerical simulation, the temperature and salinity were set to 25 °C and 35‰, respectively, and then an ocean–water dielectric constant of the ocean surface was obtained as (9.45–17.41j) at 77 GHz. For sea surface experiments, the dielectric constant needs to be adjusted by considering the temperature and salinity in the real world.

In general, for Gaussian anisotropic surfaces, the joint probability distribution of slopes can be written as

$$P(X,Y) = \frac{1}{2\pi\sqrt{mss_x}\sqrt{mss_y}} exp[-\frac{1}{2}(X^2 + Y^2)] \tag{9}$$

where mss_x and mss_y are mean square slopes in x and y directions. mss_x, mss_y, X, and Y are defined as

$$\begin{aligned}mss_x &= \int_0^{k_d}\int_0^{2\pi} k^2 cos^2\varphi\psi(k,\varphi)kdkd\varphi \\ mss_y &= \int_0^{k_d}\int_0^{2\pi} k^2 sin^2\varphi\psi(k,\varphi)kdkd\varphi\end{aligned} \tag{10}$$

$$X = \frac{tan\theta cos\varphi}{\sqrt{mss_x}}, Y = \frac{tan\theta sin\varphi}{\sqrt{mss_y}} \tag{11}$$

where k_d is the cutoff wave number; k is the wave number value; φ is the azimuth angle along the x-axis; and $\psi(k,\varphi)$ represents the two-dimensional spectrum of surface waves.

In the anisotropic case of the Gaussian surface, the NRCS of sea surfaces can be written as

$$\sigma^0_{QS}(\theta,\varphi) = \frac{|R|^2}{2\sqrt{mss_x}\sqrt{mss_y}} sec^4(\theta) exp[-\frac{1}{2}(X^2 + Y^2)]. \tag{12}$$

The NRCS in the expression (12) deviates fast from the actual NRCS when the incidence angle increases. To extend its domain of validity, the GO4 model was proposed by Boisot et al. [27]. In the simple omnidirectional Gaussian ocean surfaces, it is shown by

$$\begin{aligned}\sigma^0_{GO4}(\theta,\varphi) = &\frac{|R|^2}{mss} sec^4(\theta) exp[-\frac{tan^2(\theta)}{mss}] \\ &\times [1 + \frac{msc}{16K_0^2 mss^2 cos^2(\theta)}(\frac{tan^4(\theta)}{mss^2} - 4\frac{tan^2(\theta)}{mss} + 2)]\end{aligned} \tag{13}$$

where $mss = \int k^2 S(k)dk$ is the total mean square slope of ocean surfaces, and $mss = mss_x + mss_y$. K_0 is the incident electromagnetic wave number; $msc = \int k^4 S(k)dk$ represents the total mean square curvature of sea surfaces; and $S(k)$ represents the omnidirectional wave number spectrum.

In the anisotropic case for the Gaussian sea surfaces, the NRCS of sea surfaces in Equation (13) can be estimated as

$$\begin{aligned}\sigma^0_{GO4}(\theta,\varphi) =& \frac{|R|^2}{2\sqrt{mss_x}\sqrt{mss_y}} sec^4(\theta) exp[-\frac{1}{2}(X^2+Y^2)] \\ &\times \{1+\frac{1}{96K_0^2 cos^2(\theta)}[\frac{6msc_{xy}}{mss_x mss_y}H_2(X)H_2(Y) \\ &+\frac{msc_x}{mss_x{}^2}H_4(X)+\frac{msc_y}{mss_y{}^2}H_4(Y)]\}\end{aligned} \tag{14}$$

where msc_x, msc_y, and msc_{xy} are the directional curvatures of the ocean surface, which can be written as

$$\begin{aligned} msc_x &= \int_0^{k_d}\int_0^{2\pi} k^4 cos^4\varphi\psi(k,\varphi)kdkd\varphi \\ msc_y &= \int_0^{k_d}\int_0^{2\pi} k^4 sin^4\varphi\psi(k,\varphi)kdkd\varphi \\ msc_{xy} &= \int_0^{k_d}\int_0^{2\pi} k^2 cos^2\varphi k^2 sin^2\varphi\psi(k,\varphi)kdkd\varphi \end{aligned} \tag{15}$$

and H_n is the Hermite polynomials of order n:

$$H_n(u) = (-1)^n e^{\frac{u^2}{2}}\frac{d^n}{du^n}e^{-\frac{u^2}{2}}. \tag{16}$$

3.2. Wave Spectrum

A reliable model describing a wind-generated ocean surface is the basis for studying the MMW ocean surface scattering. The ocean wave spectrum is often used to describe some statistical parameters of the sea surface, such as mean square slope and mean square curvature, and those parameters are devoted to evaluating the abilities of scattering models (e.g., the QS model and the GO4 model). In general, the two-dimensional roughness spectrum can be described as $\psi(k,\varphi) = \frac{1}{k}S(k)\Phi(k,\varphi)$, where $\Phi(k,\varphi)$ is the angular spreading function.

In this paper, the Hwang spectrum (by Hwang et al.) and the Kudryavtsev spectrum (by Kudryavtsev et al.) are considered. For simplicity, we named two spectra by using the first author of the reference publication. In paper [40], Hwang et al. presented a new wave spectrum to study the wave spectra of small-scale waves; in our research, the corrected version of the Hwang spectrum in the 2015 paper [41] (H spectrum) is used, and the omnidirectional spectrum of the curvature is presented in (17). The H spectrum was used to estimate the scattering signature of ocean remote sensing at W band by Battaglia et al. [33]. The Kudryavtsev spectrum was first proposed in [42] and relies on the energy balance equation. We have used the Kudryavtsev spectral model in our simulations, as presented in [43] (K spectrum), and the model of the wave spectrum is given in (18). The angular spreading function is described as $\Phi(k,\varphi) = \frac{1}{2\pi}[1+\Delta(k)cos(2\varphi)]$, and $\Delta(k)$ is estimated by the method in [44].

$$B(u^*,k) = A(k)(\frac{u^*}{c(k)})^{a(k)} \tag{17}$$

where u^* is the friction velocity; $c(k)$ is the wave phase velocity; $A(k)$ and $a(k)$ are the analytical functions by developing three wave number branches [40,41].

$$B(k) = B_{lw}(k) * \exp(h(k)) + B_{eq}(k)(1-\exp(h(k))) \tag{18}$$

where B_{lw} is the long wave part of the spectrum; $h(k)$ is the cutoff term used by Elfouhaily et al. [44]; B_{eq} is the short wave spectrum established by Kudryavtsev et al.; and the details of B_{lw} and B_{eq} can be found in [42,43].

The relation between $B(k)$ and $S(k)$ is

$$B(k) = k^3 S(k). \tag{19}$$

4. Results and Discussion

4.1. Simulation Results of Scattering Models

4.1.1. σ^0 Versus Incidence Angles

In numerical simulations, it was suggested that the cutoff wave numbers were chosen to be one-tenth to one-fifth of the short wave number under consideration [45]. The validity conditions [46] of the scattering models for the large-scale surfaces are described as $< R_c > \geq \lambda$, where $< R_c >$ is the average radius of the sea surface curvature. Based on the sea wave spectrum model, it can also be rewritten as $\frac{1}{\sqrt{\int_0^{k_d}\int_0^{2\pi} k^4 \psi(k,\varphi) k dk d\varphi}} \geq \lambda$. If $\psi(k,\varphi)$ is given, the cutoff wave number k_d would be obtained. In this study, for the QS model, a cutoff wave number $k_d = K_0/10$ was used to obtain the slope parameters (mss_x and mss_y). For the GO4 model, the parameters mss_x and mss_y were estimated using the total sea surface slopes mss in the x and y directions, respectively. The curvature parameters msc_x, msc_y, and msc_{xy} were approximately calculated with a cutoff at the incident wave number K_0 [23].

The performances of the QS and the GO4 models were evaluated in the Gaussian case by adopting two different ocean wave spectrum models (i.e., the H spectrum and K spectrum). The surface condition corresponds to sea states with the H_s of 0.31 m, 0.63 m, 0.94 m, and 1.26 m. Figure 7 presents the σ calculated from the anisotropic Gaussian sea surfaces in the 77 GHz frequency band by the H spectrum in upwind and crosswind directions. The red solid line with dots, the green line with squares, the blue line with triangles, and the magenta line with stars represent the results obtained by the QS and the GO4 models with different sea states, respectively. The results from the two scattering models indicate that the strongest backscattering of the sea surface is obtained at vertical incidence, and the NRCS reduces with increasing incidence angles over an incidence range of $0 \sim 16^\circ$. At about an incidence angle of 10°, called the transition point [38], the scattering coefficient is nearly insensitive to sea states (H_s). In addition, when the incidence angle is smaller than near 10°, the scattering coefficient decreases with increasing sea states. The simulated results from two scattering models using the H spectrum have a similar conclusion to the K spectrum (as shown in Figure 8).

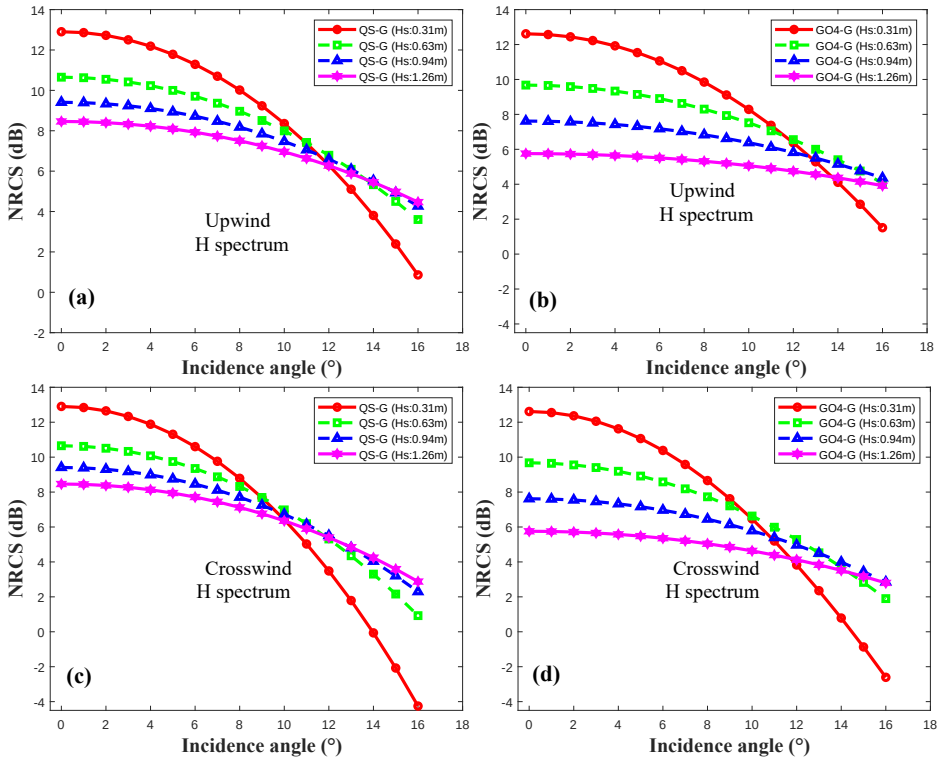


Figure 7. The simulated NRCS from two theoretical electromagnetic scattering models versus incidence angle with four sea states (H_s) in the 77 GHz frequency band. (**a**) Results from the Gaussian QS (QS-G) model in the upwind direction. (**b**) Results from the Gaussian GO4 (GO4-G) model in the upwind direction. (**c**) Results from the QS model in the crosswind direction. (**d**) Results from the GO4 mode in the crosswind direction.

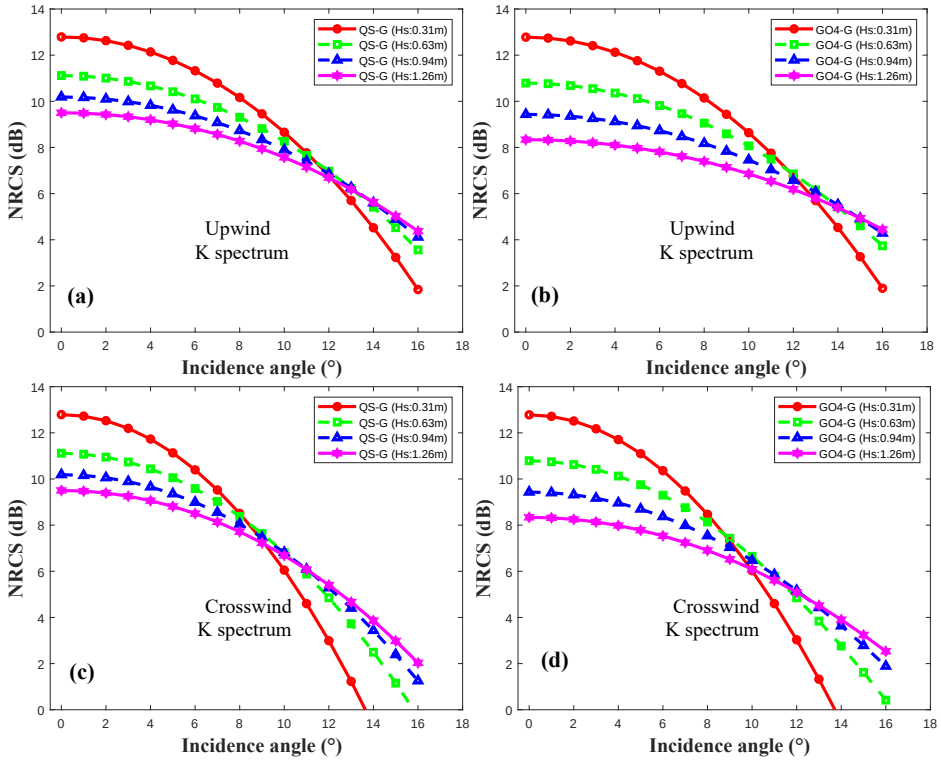


Figure 8. The simulated NRCS from two scattering models versus incidence angle with four sea states (H_s) in the 77 GHz frequency band. (**a**) Results from the QS model in the upwind direction. (**b**) Results from the GO4 model in the upwind direction. (**c**) Results from the QS model in the crosswind direction. (**d**) Results from the GO4 mode in the crosswind direction.

4.1.2. σ^0 Versus Sea States

Figure 9 presents the simulated σ versus sea states (H_s) using two scattering models at different incidence angles (i.e., 5°, 10°, and 15°) in upwind and crosswind directions. The line with dots and the curve with triangles represent the results obtained from the QS model and the GO4 model, respectively. At the incidence of 10°, the scattering coefficient has no significant difference with the rise in H_s. For the range of the low H_s (e.g., smaller than the H_s of 0.8 m), at the incidence angle of 5°, the simulated σ^0 has a tendency to decrease with the increase in H_s, while having a positive correlation with 15° incidence. Moreover, the simulated σ^0 has a weak sensitivity at moderate and high H_s. Nevertheless, as the H_s increases, the results obtained from the QS model are seen to be different from the GO4 model at three incidence angles. On the whole, the results obtained from two theoretical scattering models have a similar conclusion by employing different ocean wave spectra. Based on Equations (12) and (14), the GO4 model can be rewritten as

$$\sigma^0_{GO4}(\theta,\varphi) = \sigma^0_{QS}(\theta,\varphi) \times \{1 + \frac{1}{96K_0^2 cos^2(\theta)}[\frac{6msc_{xy}}{mss_x mss_y} H_2(X)H_2(Y) + \frac{msc_x}{{mss_x}^2} H_4(X) + \frac{msc_y}{{mss_y}^2} H_4(Y)]\}. \quad (20)$$

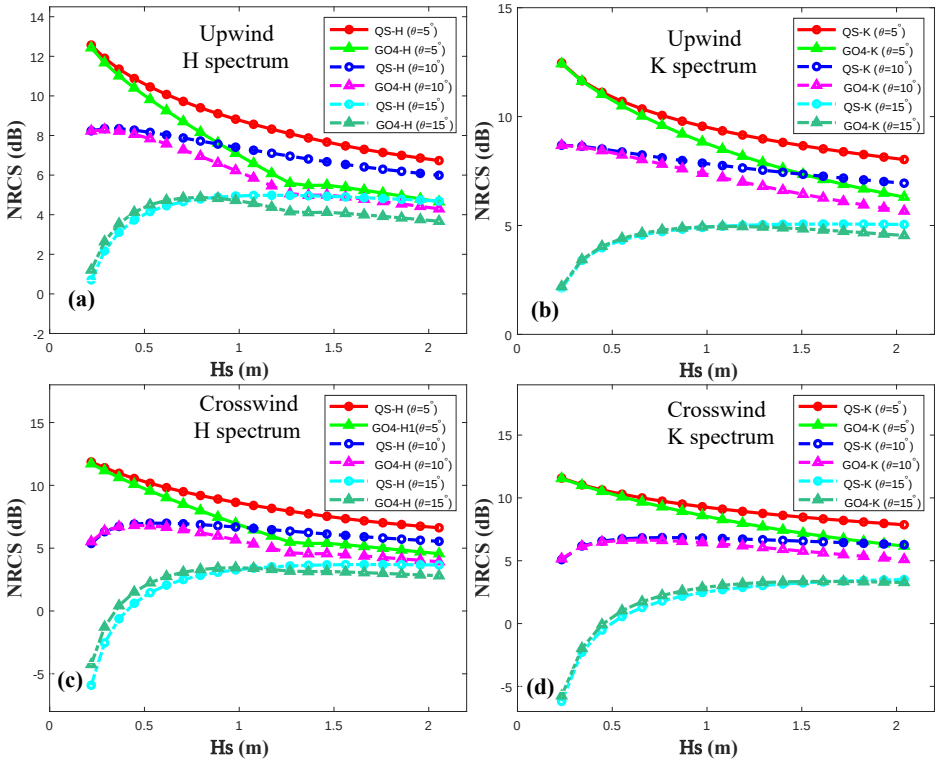


Figure 9. The NRCS versus the H_s under three incidence angles (5°, 10°, and 15° incidence angles) for two sea spectrum models. (**a**) Results from the H spectrum in upwind directions. (**b**) Results from the K spectrum in upwind directions. (**c**) Results from the H spectrum in crosswind directions. (**d**) Results from the K spectrum in crosswind directions.

Compared to the QS model, the effect of sea surface curvature (msc_{xy}, msc_x, and msc_y) was considered in the GO4 model. As the sea state rises, the contribution of the scattering

from the ocean surface curvature also changes. We define the error *err* between the GO4 model and the QS model as

$$\begin{aligned} err &= |\sigma^0_{GO4} - \sigma^0_{QS}| \\ &= |\sigma^0_{QS} \times \frac{1}{96K_0^2 cos^2(\theta)} [\frac{6msc_{xy}}{mss_x mss_y} H_2(X)H_2(Y) + \frac{msc_x}{mss_x{}^2} H_4(X) + \frac{msc_y}{mss_y{}^2} H_4(Y)]|. \end{aligned} \quad (21)$$

Figure 10 shows the error *err* from two scattering models as a function of the H_s using the K spectrum. At 5° and 10°, the errors would rise with the increase in H_s, while there are no remarkable changes at 15° incidence (<0.5 dB). In other words, at 5° and 10° incidences, the effect of the sea surface curvature has a tendency to increase with the increase in H_s, and the contribution of the scattering from the curvature becomes more important. At an angle of about 15°, the effect of the sea surface curvature is relatively stable.

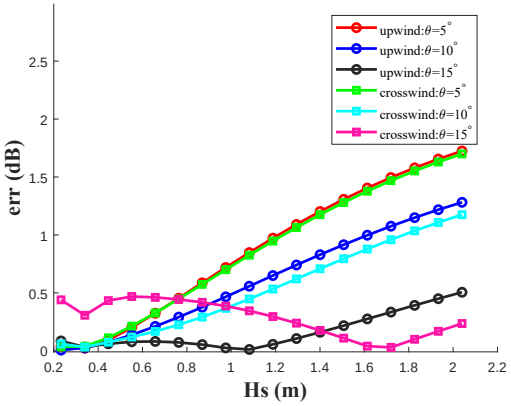


Figure 10. The error *err* as a function of H_s using the K spectrum. Curves with circles and squares represent the results in upwind and crosswind directions.

4.1.3. σ^0 Versus Azimuth Angles

Not only sea states, but also the relative direction between the radar antenna beam and the wave direction affects σ^0. Figure 11 shows the estimated scattering coefficients versus azimuth angles under two sea state cases (the H_s of 0.45 m and 1.08 m) at the incidence angles of 5°, 10°, and 15°, respectively. The red solid line, the black dotted lines, the blue line with dots, and the magenta chain-dotted lines represent the results obtained from the QS and the GO4 models with the H spectrum and K spectrum, respectively. The scattering coefficient changes approximately periodically with the range of $0 \sim 360°$. The simulated results clearly demonstrate the maxima around 0°/360° and 180° as well as the minima around 90° and 270°. The observed asymmetry of the upwind/crosswind direction can be as high as about 2.5 dB at 15° incidence with the H_s of 0.45 m, while about 0.3 dB for 5° incidence. At large incidence angles, a marked upwind–crosswind asymmetry is observed. The simulated results from the H_s of 0.45 m have a similar conclusion to the H_s of 1.08 m using two different ocean wave spectrum models. Figure 12 gives the error *err* (as in Equation (21)) versus azimuth angles with the H_s of 0.45 m using the H spectrum. At 15° incidence, the effect of the sea surface curvature varies with azimuth angles, and the maximum error is about 0.9 dB, while the effect of the sea surface curvature is close to a constant (approximately 0.47 dB) at 5° incidence. To sum up, the scattering contribution from the sea surface curvature is affected by azimuth angles at the high incidence angle.

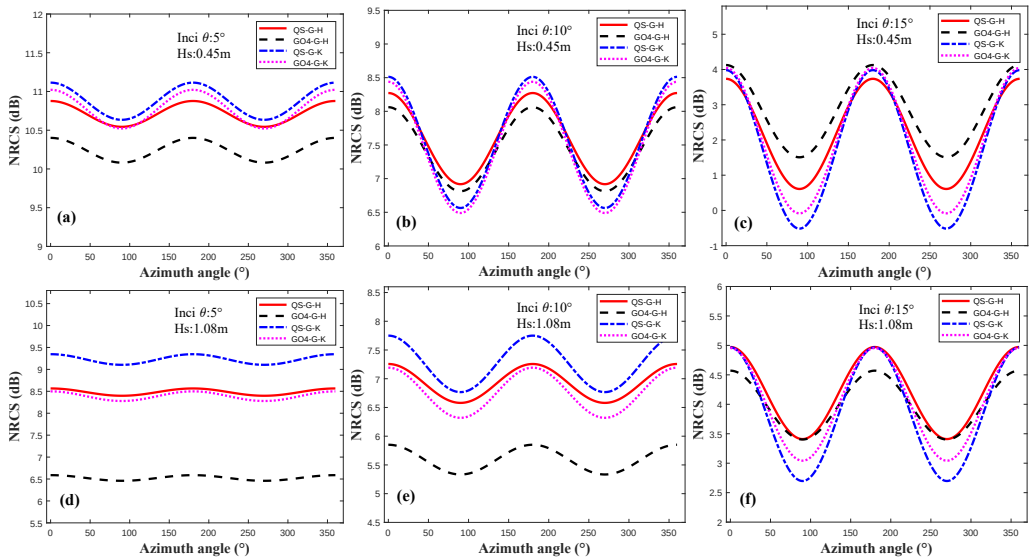


Figure 11. The simulated NRCS versus azimuth angles with two sea states in the 77 GHz frequency band by the H spectrum and K spectrum, at different incidence angles. (**a**–**c**) Results from the H_s of 0.45 m at 5° incidence, 10° incidence, and 15° incidence. (**d**–**f**) Results from the H_s of 1.08 m.

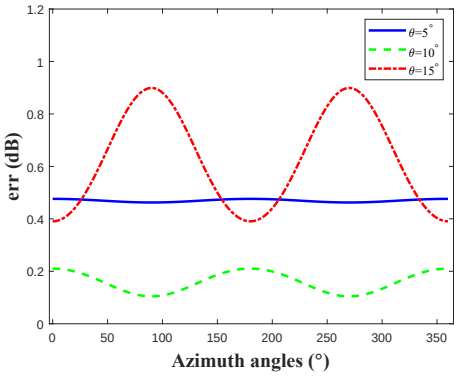


Figure 12. The error *err* as a function of azimuth angles using the H spectrum. The blue solid line, the green dotted line, and red dotted line represent the results obtained from the 5°, 10°, and 15° incidences, respectively.

4.2. Comparison with Experimental Data

4.2.1. Ocean Data

Figure 13 shows the NRCS versus incidence angles with the H_s of 0.33 m, 0.40 m, 0.43 m, 0.48 m, 0.52 m, and 0.63 m in upwind directions, and the obtained results were compared with the simulation by using two scattering models and two wave spectrum models. Errorbars are ±1 standard deviation. The red squares, the blue solid line, the green dotted line, the cyan solid line, and the magenta dotted line represent the results obtained from the ocean surface, the QS model, and the GO4 model by employing the H spectrum and K spectrum, respectively. In Figure 13, it can be seen that the measured NRCS decreases with increasing incidence angles; the NRCS obtained from the H_s of 0.33 m reduces to about 11.5 dB over an incidence range of $0 \sim 16°$; and the variation in the NRCS is about 5.5 dB for the H_s of 0.63 m. In addition, the abilities of the QS model and GO4 model to reproduce the small-incidence NRCS are shown for the 77 GHz frequency band in near-nadir-radar observations. As shown in Figure 13, the QS model and GO4 model are found to be in overall good agreement with the experimental data over an incidence range of $0 \sim 12°$. Nevertheless, two scattering models would depart from the measured NRCS as the incidence angle grows (>12°). As is well known, for the transition range of

incidence angles ($10^\circ \sim 20^\circ$ [21]), Bragg scattering also contributes to the scattered energy for the sea surface scattering. The only specular scattering model cannot well describe the scattering mechanism of the transition region, while the new model that is combined with Bragg scattering may be a suitable method, and this will be one of our future works.

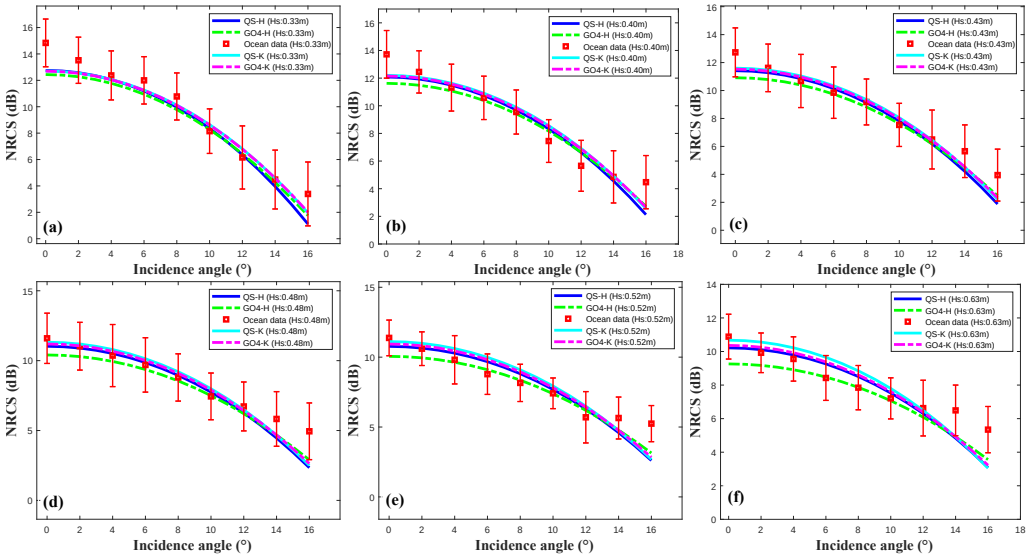


Figure 13. The obtained NRCS versus incidence angles with six sea states in upwind directions. (**a**) Ocean surfaces with the H_s of 0.33 m. (**b**) Ocean surfaces with the H_s of 0.40 m. (**c**) Ocean surfaces with the H_s of 0.43 m. (**d**) Ocean surfaces with the H_s of 0.48 m. (**e**) Ocean surfaces with the H_s of 0.52 m. (**f**) Ocean surfaces with the H_s of 0.63 m. Errorbars are ± 1 standard deviation.

The scattering coefficient (in upwind directions) obtained from ocean surface measurements under different sea states is shown in Figure 14. Errorbars are ± 1 standard deviation. The red line with dots, the blue line with squares, the green line with triangles, the black line with rhombuses, the magenta line with pentagrams, and the cyan line with hexagrams represent the results obtained from the H_s of 0.33 m, 0.40 m, 0.43 m, 0.48 m, 0.52 m, and 0.63 m, respectively. The preliminary conclusion of this result is that the scattering coefficient is nearly insensitive to low sea states for a small range of incidence angles of about 10° in ocean observations, and the results of the ocean observation correspond to the simulation results from two scattering models. When the incidence angle is smaller than about 10°, the scattering coefficient is sensitive to sea surface conditions. One possible reason is that, as the sea surface roughness increases with rising sea states, the number of specular facets reduce; as a result, the scattering coefficient would decrease.

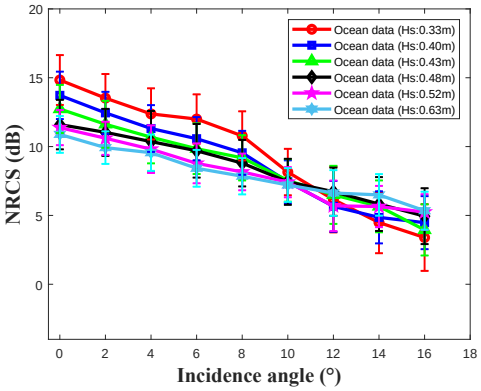


Figure 14. Comparison of the NRCS (in dB) obtained from the upwind directions in near-nadir-radar sea surface observations. The H_s of six datasets are 0.33 m, 0.40 m, 0.43 m, 0.48 m, 0.52 m, and 0.63 m, respectively. Errorbars are ± 1 standard deviation.

4.2.2. Wave Tank Data

In wave tank experiments, three sets of irregular wave water surfaces were first produced, and the measured NRCS is given in Figure 15a. The curve with dots represents the obtained results from the H_s of 0.16 m, while the curves with squares and triangles depict the results from the H_s of 0.19 m and 0.24 m, respectively. Overall, the NRCS from irregular wave water surfaces decreased with increasing incidence angles. When the incidence angle is greater than about 10°, the NRCS shows a dramatic reduction. In addition, the obtained NRCS from three H_s have no significant difference, and the possible reason is that the generated water surfaces in this experiment are close. For wave tank experiments with regular waves, Figure 15b displays the NRCS versus incidence angles by processing the collected radar data. Similar to irregular waves, the measured σ^0 reduces as the incidence angle grows. Moreover, over the incidence range of $0 \sim 16°$, the phenomenon from the regular wave water surfaces is found to be in overall good agreement with the irregular waves.

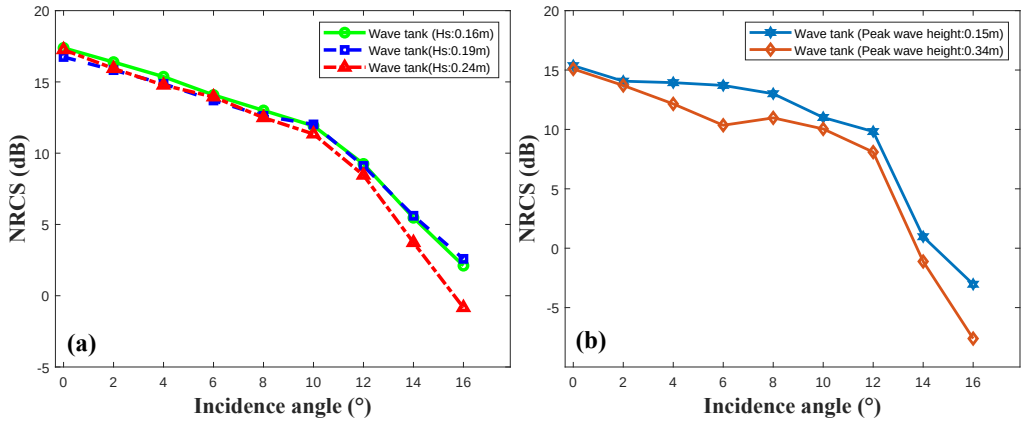


Figure 15. The obtained NRCS from the wave tank observation in the upwind direction. (**a**) The irregular wave water surfaces. (**b**) The wave tank experiments with regular waves.

As seen in Figure 15, the scattering coefficient changes slowly with the range of $0 \sim 10°$, while σ_0 has a rapid reduction over the incidence angle of $12 \sim 16°$. The observed results, including irregular waves and regular waves, prove this conclusion. Compared with irregular waves, the reduction in the scattering coefficient from regular waves seems to be more obvious over the incidence angle of $12 \sim 16°$. In wave tank observations, for the irregular waves, the water surfaces were produced, which were close to the energy of the JONSWAP spectrum, while regular waves were sine-shaped waves. One possible reason for the difference in scattering characterization is that irregular wave water surfaces have specular conditions to contribute to the return at high incidence angles (>12°), and this needs to be studied further.

4.2.3. Comparison of Sea and Water Surface Return

To better characterize the difference in scattering property between sea surfaces and water, the relative NRCS is calculated by normalizing the NRCS using its maximum value. The relative difference is written as

$$\Delta(\theta) = |\sigma_{wtk}(\theta) - \sigma_{oce}(\theta)| \tag{22}$$

where $\sigma_{wtk}(\theta)$ and $\sigma_{oce}(\theta)$ are the relative NRCS obtained from water surfaces in the wave tank and oceans, respectively.

Figure 16 presents a comparison of the NRCS from ocean and water surfaces. The data obtained from the irregular wave water surfaces with the H_s of 0.24 m and sea surfaces

with the H_s of 0.43 m were used. The relative NRCS reduced with increasing incidence angles for the sea surface and wave tank observations. However, when the incidence angle was larger than about 12°, as the incidence angle rose, the variation between ocean and water surfaces was significant.

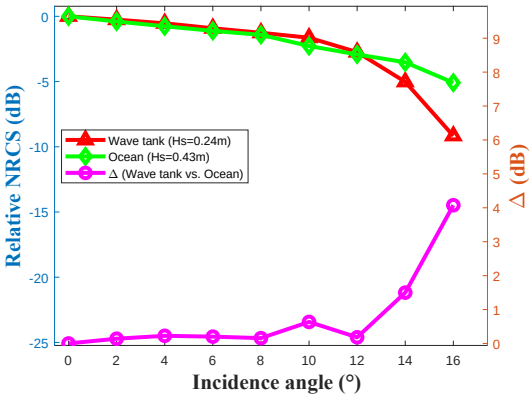


Figure 16. The relative NRCS as a function of θ for the results obtained from water and ocean surfaces in the 77 GHz frequency band. The results from two observations are shown in the red triangle line and green rhombus line, respectively. Curves with circles represent the relative difference (in dB) between the results from water and sea surfaces.

4.3. Discussion

Some observations, including wave tank and sea surfaces, and modeling of the 77 GHz frequency band scattering are combined to investigate the scattering mechanism at near vertical incidence. Some phenomena and results are given as follows:

1. At low incidence angles, the scattering coefficient of ocean surfaces reduces with increasing incidence angles in the 77 GHz frequency band. This conclusion is verified by comparing the results from the simulated NRCS and ocean surface experiments. The QS model and the GO4 model are applied to study the sea surface scattering mechanism by using the H spectrum and K spectrum; the obtained results show the performances of scattering models for the MMW ocean surface backscattering characterization. In addition, the transition point is found at approximately 10° incidence, and the results from the ocean surface observations and the wave tank prove the above conclusion.
2. The dependence of the 77 GHz sea surface scattering on sea states is investigated using the MMW radar measurements. At a small range of incidence angles near 10°, the scattering cross section is nearly insensitive to low sea states (H_s). When the incidence angle is less than the transition point, the NRCS decreases with rising sea states. The reasonable explanation is that the number of specular facets decreases while the H_s rises. Furthermore, the contribution of the scattering from the sea surface curvature becomes more important as the H_s increases ($\theta < 10°$) in numerical simulations.
3. The azimuth angles also affect the NRCS in the near-nadir-radar observations of the sea surface for the MMW frequency band. The asymmetry of the upwind–crosswind direction is observed from the obtained results by two theoretical scattering models (using the H spectrum and K spectrum). Moreover, the simulations show that the scattering contribution from the sea surface curvature is affected by the azimuth angles at high incidence angles.

The backscattering mechanism of the MMW radar return is studied in this paper. We did not systematically analyze the scattering characteristic of the wave tank from the modeling of water surfaces and numerical simulations (beyond the scope of the present study, only as a contrast), but show the obtained results from wave tank experiments.

Different from the wind–wave tank, the water surface in this study is produced from the mechanical motion of the wave generator, which has only large-scale gravity waves. For instance, the wave profile from regular waves with a peak-to-peak height of 0.34 m is presented in Figure 17. Figure 16 shows a variation between ocean surface observations (with capillary waves [45,47]) and the wave tank (only gravity waves); for example, when the incidence angle is larger than near 14°, the relative difference Δ remains more than 2 dB. We preliminary verify that the Bragg scattering is becoming more and more significant in near-nadir sea surface observations at the transition range of incidence angles, and this phenomenon needs further research based on the theoretical electromagnetic scattering model and the datasets of radar observations, including the wave tank and the oceans.

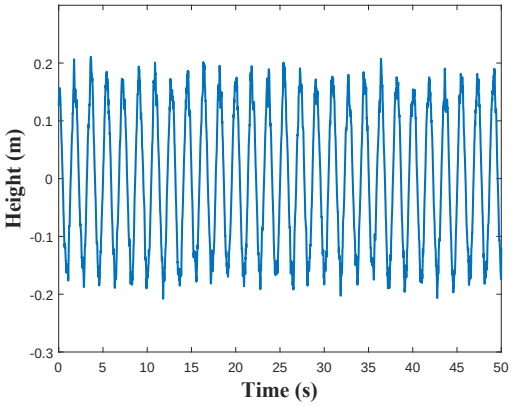


Figure 17. Wave profile from regular waves in the wave tank.

In fact, due to the complexity of the six-degree-of-freedom motion and the accuracy of the sensor, the obtained NRCS in this paper was not precise enough. In addition, because of the measurement environment limitation (such as the safe navigation of the UAV under bad weather and strong wind conditions), we do not have enough datasets, including the azimuth angle datasets and mid-high-sea states. As a result, we can only provide some preliminary results for low-sea-state ocean observations at this time, and the dependence of the sea surface NRCS on azimuth angles and mid-high-sea states cannot be verified in this paper. The sea-based fixed platform, such as marine drilling platforms, would be considered for installing the MMW radar, and a long-term observation would be carried out to further evaluate the characterization of the MMW backscattering from sea surfaces.

5. Conclusions

In this article, we investigated the characterization of the 77 GHz frequency band in near-nadir-radar observations. The scattering coefficient for the oceans was first described by employing the QS model and the GO4 model, and some ocean surface observations were carried out by using a MMW radar. We analyzed the dependence of the 77 GHz frequency band backscatter on different conditions, i.e., incidence angles, azimuth angles, and sea states (H_s), and the related conclusions were confirmed by comparing the results obtained from the MMW radar data (i.e., wave tank and oceans) and the simulation (i.e., the QS model and the GO4 model). The obtained results demonstrated the performances of two scattering models for the ocean surface scattering mechanism in the 77 GHz frequency band. At low incidence angles, the scattering coefficient decreases while the incidence angle increases. As the sea surface roughness rises with increasing sea states, the specular scattering decreases. The asymmetry of the upwind–crosswind direction was also observed based on numerical simulations. In addition, the dependence of the sea surface curvature on sea states (H_s) and azimuth angles was analyzed by combining two scattering models

and two wave spectra. The obtained results can provide new insights for the understanding of how MMW radar backscatter and surface dynamic environment interact.

Although the measured results from sea surfaces are preliminary, they improve the knowledge for the characterization of the MMW sea surface backscattering at low incidence angles. The study of the scattering mechanism is of great value to assess the performance of the scattering model and further improve the accuracy of the model. Based on the scattering models (e.g., the QS model and the GO4 model), wave spectra would be extracted by using the collected radar returns, and then sea surface wind speeds and wave parameters would be retrieved.

In future work, a long-term observation by combining the MMW radar and the wave buoy would be conducted to further study the ocean surface backscattering mechanism, especially in mid-high-sea conditions. In addition, the Bragg scattering in the 77 GHz frequency band would be studied. As is well known, for moderate incidence angles, the backscattering mechanism from the sea surface is dominated by Bragg scattering. Based on the Bragg resonance theory, the incident electromagnetic wave has a significant influence on the sea surface scattering mechanism. The electromagnetic wavelength of the 77 GHz frequency band (≈3.9 mm) is shorter than low microwave bands, e.g., the X band (≈3 cm) and the Ku band (≈2 cm). Due to the dominant role of the small-scale waves, the physics involved in describing sea surfaces and the scattering mechanism is different from that considered in usual models. For example, the results from the paper [33] show that the observations do not have a significant polarization dependence at the W band. Therefore, the research of the Bragg scattering mechanism based on the MMW radar is of great potential for explaining new phenomena on the sea surface and high temporal–spatial measurements.

Author Contributions: Conceptualization, Q.X. and C.Z.; methodology, Q.X., C.Z. and S.W.; software, Q.X. and X.W.; formal analysis, Q.X. and S.W.; validation, C.Z., Z.C. and L.F.; writing—original draft preparation, Q.X.; supervision, C.Z.; project administration, C.Z., Z.C. and L.F.; funding acquisition, C.Z. and Z.C. All authors have read and agreed to the published version of the manuscript.

Funding: This work was supported in part by the National Natural Science Foundation of China under grant no. 42276190 and grant no. 61871296, and in part by the Science Foundation of Donghai Laboratory under grant no. DH-2022KF01020.

Data Availability Statement: The original contributions presented in the study are included in the article, the authors do not have permission to share data.

Conflicts of Interest: The authors declare no conflicts of interest.

References

1. Saad, W.; Bennis, M.; Chen, M. A vision of 6G wireless systems: Applications, trends, technologies, and open research problems. *IEEE Netw.* **2019**, *34*, 134–142. [CrossRef]
2. Patole, S.M.; Torlak, M.; Wang, D.; Ali, M. Automotive radars: A review of signal processing techniques. *IEEE Signal Process. Mag.* **2017**, *34*, 22–35. [CrossRef]
3. Ding, F.; Zhao, C.; Chen, Z.; Li, J. Sea Echoes for Airborne HF/VHF Radar: Mathematical Model and Simulation. *Remote Sens.* **2020**, *12*, 3755. [CrossRef]
4. Liu, H.; Chen, Z.; Zhao, C. A new Doppler model incorporated with free and broken-short waves for coherent S-band wave radar at near-grazing angles. *IEEE Trans. Geosci. Remote Sens.* **2021**, *60*, 1–11. [CrossRef]
5. Wu, S.; Zhao, C.; Chen, Z.; Wang, X.; Zhang, C.; Wei, Y. A New Doppler Model for Shipboard Coherent Microwave Ocean Radar. *IEEE Trans. Geosci. Remote Sens.* **2023**, *61*, 1–13. [CrossRef]
6. He, J.; Chen, Z.; Zhao, C.; Chen, X.; Wei, Y.; Zhang, C. A New Method to Suppress Non-Wave Components in Sea Echoes of Coherent Microwave Radar Based on Radon Transform and Fourier Transform. *IEEE Trans. Geosci. Remote Sens.* **2022**, *60*, 1–10. [CrossRef]

7. Zhao, C.; Wang, X.; Chen, Z.; Wu, S.; Zeng, Y. Inversion of Wave Parameters From Time-Doppler Spectrum Using Shore-Based Coherent S-Band Radar. *IEEE Trans. Geosci. Remote Sens.* **2023**, *61*, 1–11. [CrossRef]
8. Giovanangeli, J.P.; Bliven, L.F.; Le Calve, O. A wind-wave tank study of the azimuthal response of a Ka-band scatterometer. *IEEE Trans. Geosci. Remote Sens.* **1991**, *29*, 143–148. [CrossRef]
9. Gade, M.; Alpers, W.; Ermakov, S.A.; Hühnerfuss, H.; Lange, P.A. Wind-wave tank measurements of bound and freely propagating short gravity-capillary waves. *J. Geophys. Res. Oceans* **1998**, *103*, 21697–21709. [CrossRef]
10. Plant, W.J.; Keller, W.C.; Hesany, V.; Hara, T.; Bock, E.; Donelan, M.A. Bound waves and Bragg scattering in a wind-wave tank. *J. Geophys. Res. Oceans* **1999**, *104*, 3243–3263. [CrossRef]
11. Chen, P.; Wang, X.; Liu, L.; Chong, J. A coupling modulation model of capillary waves from gravity waves: Theoretical analysis and experimental validation. *J. Geophys. Res. Oceans* **2016**, *121*, 4228–4244. [CrossRef]
12. Smirnov, A.V.; Fuks, I.M.; Naugolnykh, K.A. Crosswind ocean radar backscatter and two-scale scattering model at low grazing angles. *Radio Sci.* **2003**, *38*, 1–8. [CrossRef]
13. Ryabkova, M.; Karaev, V.Y.; Titchenko, Y.A.; Meshkov, E. Experimental study of the microwave radar Doppler spectrum backscattered from the sea surface at low incidence angles. In Proceedings of the 2017 XXXIInd General Assembly and Scientific Symposium of the International Union of Radio Science (URSI GASS), Montreal, QC, Canada, 19–26 August 2017; pp. 1–4.
14. Yurovsky, Y.Y.; Kudryavtsev, V.N.; Grodsky, S.A.; Chapron, B. Sea surface Ka-band Doppler measurements: Analysis and model development. *Remote Sens.* **2019**, *11*, 839. [CrossRef]
15. Masuko, H.; Okamoto, K.; Shimada, M.; Niwa, S. Measurement of microwave backscattering signatures of the ocean surface using X band and Ka band airborne scatterometers. *J. Geophys. Res. Oceans* **1986**, *91*, 13065–13083. [CrossRef]
16. Tanelli, S.; Durden, S.L.; Im, E. Simultaneous measurements of Ku-and Ka-band sea surface cross sections by an airborne radar. *IEEE Geosci. Remote Sens. Lett.* **2006**, *3*, 359–363. [CrossRef]
17. Fjørtoft, R.; Gaudin, J.M.; Pourthié, N.; Lalaurie, J.C.; Mallet, A.; Nouvel, J.F.; Martinot-Lagarde, J.; Oriot, H.; Borderies, P.; Ruiz, C.; et al. KaRIn on SWOT: Characteristics of near-nadir Ka-band interferometric SAR imagery. *IEEE Trans. Geosci. Remote Sens.* **2013**, *52*, 2172–2185. [CrossRef]
18. Nouguier, F.; Chapron, B.; Collard, F.; Mouche, A.A.; Rascle, N.; Ardhuin, F.; Wu, X. Sea surface kinematics from near-nadir radar measurements. *IEEE Trans. Geosci. Remote Sens.* **2018**, *56*, 6169–6179. [CrossRef]
19. Plant, W.J.; Dahl, P.H.; Keller, W.C. Microwave and acoustic scattering from parasitic capillary waves. *J. Geophys. Res. Oceans* **1999**, *104*, 25853–25866. [CrossRef]
20. Plant, W.J.; Dahl, P.H.; Giovanangeli, J.P.; Branger, H. Bound and free surface waves in a large wind-wave tank. *J. Geophys. Res. Oceans* **2004**, *109*, C10002. [CrossRef]
21. Karaev, V.Y.; Titchenko, Y.A.; Meshkov, E.; Panfilova, M. Microwave backscattering by the sea surface in the transition range of incidence angles (10°–20°): Theory and experiment. In Proceedings of the 2017 Progress in Electromagnetics Research Symposium-Fall (PIERS-FALL), Singapore, 19–22 November 2017; pp. 2183–2188.
22. Bringer, A.; Guérin, C.A.; Chapron, B.; Mouche, A.A. Peakedness effects in near-nadir radar observations of the sea surface. *IEEE Trans. Geosci. Remote Sens.* **2012**, *50*, 3293–3301. [CrossRef]
23. Boisot, O.; Pioch, S.; Fatras, C.; Caulliez, G.; Bringer, A.; Borderies, P.; Lalaurie, J.C.; Guérin, C.A. Ka-band backscattering from water surface at small incidence: A wind-wave tank study. *J. Geophys. Res. Oceans* **2015**, *120*, 3261–3285. [CrossRef]
24. Hwang, P.A.; Ainsworth, T.L.; Ouellette, J.D. Microwave specular measurements and ocean surface wave properties. *Sensors* **2021**, *21*, 1486. [CrossRef] [PubMed]
25. Yan, Q.; Zhang, J.; Fan, C.; Meng, J. Analysis of Ku-and Ka-band sea surface backscattering characteristics at low-incidence angles based on the GPM dual-frequency precipitation radar measurements. *Remote Sens.* **2019**, *11*, 754. [CrossRef]
26. Valenzuela, G.R. Theories for the interaction of electromagnetic and oceanic waves—A review. *Bound. Layer Meteor.* **1978**, *13*, 61–85. [CrossRef]
27. Boisot, O.; Nouguier, F.; Chapron, B.; Guérin, C.A. The GO4 model in near-nadir microwave scattering from the sea surface. *IEEE Trans. Geosci. Remote Sens.* **2015**, *53*, 5889–5900. [CrossRef]
28. Li, J.; Zhang, M.; Zhao, Y.; Jiang, W. Efficient numerical full-polarized facet-based model for EM scattering from rough sea surface within a wide frequency range. *Remote Sens.* **2019**, *11*, 75. [CrossRef]
29. Yurovsky, Y.Y.; Kudryavtsev, V.N.; Grodsky, S.A.; Chapron, B. Ka-band dual copolarized empirical model for the sea surface radar cross section. *IEEE Trans. Geosci. Remote Sens.* **2016**, *55*, 1629–1647. [CrossRef]
30. Yurovsky, Y.Y.; Kudryavtsev, V.N.; Grodsky, S.A.; Chapron, B. Ka-band radar cross-section of breaking wind waves. *Remote Sens.* **2021**, *13*, 1929. [CrossRef]
31. Horie, H.; Kuroiwa, H.; Kumagai, H. Near nadir scattering properties at W-band frequency for the sea surface. In Proceedings of the IGARSS 2004. 2004 IEEE International Geoscience and Remote Sensing Symposium, Anchorage, AK, USA, 20–24 September 2004; Volume 3, pp. 1742–1745.

32. Li, L.; Heymsfield, G.M.; Tian, L.; Racette, P.E. Measurements of ocean surface backscattering using an airborne 94-GHz cloud radar—Implication for calibration of airborne and spaceborne W-band radars. *J. Atmos. Ocean Technol.* **2005**, *22*, 1033–1045. [CrossRef]
33. Battaglia, A.; Wolde, M.; D'Adderio, L.P.; Nguyen, C.; Fois, F.; Illingworth, A.; Midthassel, R. Characterization of surface radar cross sections at W-band at moderate incidence angles. *IEEE Trans. Geosci. Remote Sens.* **2017**, *55*, 3846–3859. [CrossRef]
34. Brown, G.S. Quasi-specular scattering from the air-sea interface. In *Surface Waves and Fluxes: Volume II—Remote Sensing*; Geernaert and Plant, Ed.; Kluwer: Norwell, MA, USA, 1990; pp. 1–39.
35. Lee, W.C.; Dodge, P.; Marks, F.D., Jr.; Hildebrand, P.H. Mapping of airborne Doppler radar data. *J. Atmos. Ocean Technol.* **1994**, *11*, 572–578. [CrossRef]
36. Sapp, J.W.; Alsweiss, S.O.; Jelenak, Z.; Chang, P.S.; Frasier, S.J.; Carswell, J. Airborne co-polarization and cross-polarization observations of the ocean-surface NRCS at C-band. *IEEE Trans. Geosci. Remote Sens.* **2016**, *54*, 5975–5992. [CrossRef]
37. Barrick, D. Rough surface scattering based on the specular point theory. *IEEE Trans. Antennas Propagat.* **1968**, *16*, 449–454. [CrossRef]
38. Hesany, V.; Plant, W.J.; Keller, W.C. The normalized radar cross section of the sea at 10° incidence. *IEEE Trans. Geosci. Remote Sens.* **2000**, *38*, 64–72. [CrossRef]
39. Liu, Q.; Weng, F.; English, S.J. An improved fast microwave water emissivity model. *IEEE Trans. Geosci. Remote Sens.* **2010**, *49*, 1238–1250. [CrossRef]
40. Hwang, P.A.; Wang, D.W. An empirical investigation of source term balance of small scale surface waves. *Geophys. Res. Lett.* **2004**, *31*, L15301. [CrossRef]
41. Hwang, P.A.; Fois, F. Surface roughness and breaking wave properties retrieved from polarimetric microwave radar backscattering. *J. Geophys. Res. Oceans* **2015**, *120*, 3640–3657. [CrossRef]
42. Kudryavtsev, V.; Makin, V.; Chapron, B. Coupled sea surface-atmosphere model: 2. Spectrum of short wind waves. *J. Geophys. Res. Oceans* **1999**, *104*, 7625–7639. [CrossRef]
43. Kudryavtsev, V.; Hauser, D.; Caudal, G.; Chapron, B. A semiempirical model of the normalized radar cross-section of the sea surface 1. Background model. *J. Geophys. Res. Oceans* **2003**, *108*, FET-2. [CrossRef]
44. Elfouhaily, T.; Chapron, B.; Katsaros, K.; Vandemark, D. A unified directional spectrum for long and short wind-driven waves. *J. Geophys. Res. Oceans* **1997**, *102*, 15781–15796. [CrossRef]
45. Plant, W.J. A two-scale model of short wind-generated waves and scatterometry. *J. Geophys. Res. Oceans* **1986**, *91*, 10735–10749. [CrossRef]
46. Sultan-Salem, A.K.; Tyler, G.L. Validity of the Kirchhoff approximation for electromagnetic wave scattering from fractal surfaces. *IEEE Trans. Geosci. Remote Sens.* **2004**, *42*, 1860–1870. [CrossRef]
47. Donelan, M.A.; Pierson, W.J., Jr. Radar scattering and equilibrium ranges in wind-generated waves with application to scatterometry. *J. Geophys. Res. Oceans* **1987**, *92*, 4971–5029.

Disclaimer/Publisher's Note: The statements, opinions and data contained in all publications are solely those of the individual author(s) and contributor(s) and not of MDPI and/or the editor(s). MDPI and/or the editor(s) disclaim responsibility for any injury to people or property resulting from any ideas, methods, instructions or products referred to in the content.